Article

Head-mounted optical imaging and optogenetic stimulation system for use in behaving primates

Graphical abstract

Head-mounted optical imaging and wireless optogenetic stimulation for behaving primates

Camera

Widefield Optical Imaging

Wireless Optogenetic Stimulation

V4
V2
V1

Single Domain Stimulation

V2

V1

Behaving Macaque

Authors

Derek Zaraza, Mykyta M. Chernov,
Yiyuan Yang, John A. Rogers,
Anna W. Roe, Robert M. Friedman

Correspondence

zaraza@ohsu.edu (D.Z.),
friedmro@ohsu.edu (R.M.F.)

In brief

To study naturalistic behaviors in monkeys, Zaraza et al. develop a head-mounted imaging and wireless optogenetic stimulation device. It is small, easy to mount, and low cost. They present images of mesoscale functional domains in visual areas V1, V2, and V4 and demonstrate evidence of spatiotemporal cortical modulation induced by focal optogenetic stimulation.

Highlights

- Chamber-mounted imaging and optical stimulation device for non-head-fixed macaques

- Low cost, easy to mount, widefield (cm-size) mini camera and wireless μLED stimulator

- Provides good mesoscale functional maps in areas V1, V2, and V4

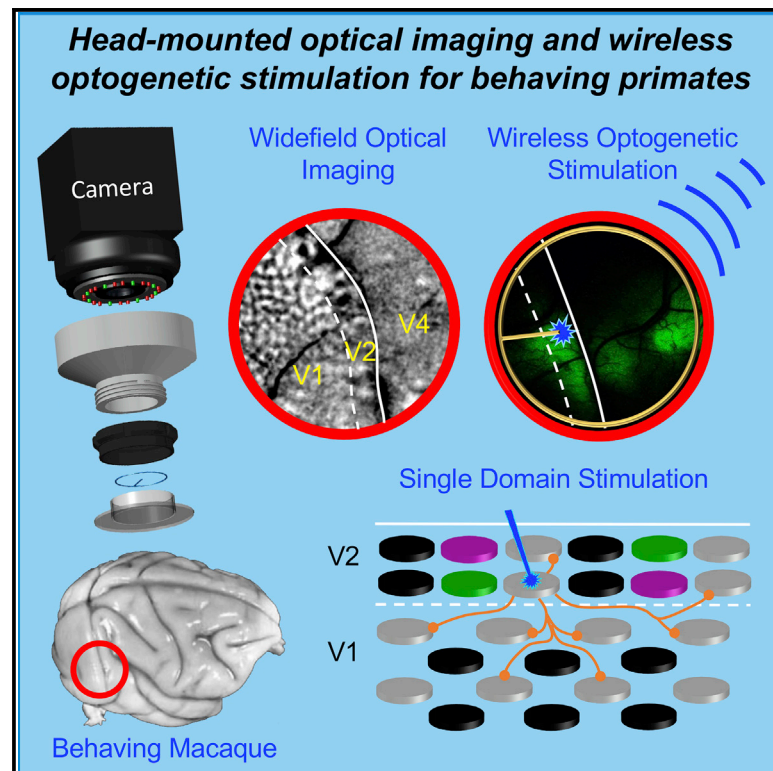- Images cortical response during optogenetic stimulation of functional domains

CellPress

Article

Head-mounted optical imaging and optogenetic stimulation system for use in behaving primates

Derek Zaraza,[1,*] Mykyta M. Chernov,[1] Yiyuan Yang,[2] John A. Rogers,[2] Anna W. Roe,[1,3,4] and Robert M. Friedman[1,4,5,*]

[1]Division of Neuroscience, Oregon National Primate Research Center, Oregon Health and Science University, Beaverton, OR 97006, USA
[2]Department of Materials Science and Engineering, Northwestern University, Evanston, IL 60208, USA
[3]Present address: Interdisciplinary Institute of Neuroscience and Technology (ZIINT), School of Medicine, Zhejiang University, Hangzhou, China
[4]Senior author
[5]Lead contact
*Correspondence: zaraza@ohsu.edu (D.Z.), friedmro@ohsu.edu (R.M.F.)
https://doi.org/10.1016/j.crmeth.2022.100351

> **MOTIVATION** Nonhuman primates remain our best animal model for studying the neural underpinnings of human behavior. Our device is an initial step toward developing a system for widefield optical imaging and stimulation in freely moving nonhuman primates. Such systems have been used to study naturalistic behaviors in rodents and other small animals, but the size of the primate brain offers unique challenges in imaging cortical areas that we address in this study.

SUMMARY

Advances in optical technology have revolutionized studies of brain function in freely behaving mice. Here, we describe an optical imaging and stimulation device for use in primates that easily attaches to an intracranial chamber. It consists of affordable commercially available or 3D-printed components: a monochromatic camera, a small standard lens, a wireless μLED stimulator powered by an induction coil, and an LED array for illumination. We show that the intrinsic imaging performance of this device is comparable to a standard benchtop system in revealing the functional organization of the visual cortex for awake macaques in a primate chair or under anesthesia. Imaging revealed neural modulatory effects of wireless focal optogenetic stimulation aimed at identified functional domains. With a 1 to 2 cm field of view, 100× larger than previously used in primates without head restraint, our device permits widefield optical imaging and optogenetic stimulation for ethological studies in primates.

INTRODUCTION

Optical investigations of neuronal brain activity in behaving animals have greatly advanced our understanding of brain function. They employ novel optical windows, imaging methods, and optogenetic stimulation. Brain imaging with a field of view (FOV) of 1 mm or smaller has been performed in freely moving animals,[1–5] usually with a small gradient refractive index (GRIN) lens-based microscope. When coupled with 1- and 2-photon optogenetic activation, neural networks underlying behavior can be studied at the cellular level.[6,7] This approach has been adapted for head-stabilized nonhuman primates (NHPs).[8–11] Larger FOV fluorescent and intrinsic signal imaging in freely moving rodents is also being developed;[12–15] however, the largest FOVs have been on the order of 5 mm.[16]

An important aspect of brain function in NHPs is the mesoscale (sub-millimeter scale) functional organization. To study the circuitry of mesoscale functional domains across multiple cortical areas, optical approaches employ large scientific cameras with tandem and macro lenses to view 1–2 cm in size cortical regions. Approaches coupling optical intrinsic signal imaging (OISI) in combination with electrical, optogenetic, and infrared neural stimulation (INS) have revealed intra- and inter-areal functional connectivity in the primary visual cortex (V1) in vivo.[17–20] Such large field imaging and stimulation approaches, however, are not yet available for studies in freely behaving NHPs. Given the importance of studying naturalistic behaviors in freely behaving NHPs (such as visual tracking and hand/eye coordination), there is a need for a head-stabilized imaging and stimulation device that provides large-scale coverage of multiple brain areas and ∼100 μm spatial resolution.

Here, we describe a small chamber-mounted device built with off-the-shelf and 3D-printed components that can be used for widefield optical imaging and optogenetic stimulation in macaque monkeys without the need for head restraint. Our device offers stimulation and imaging with an FOV that can cover
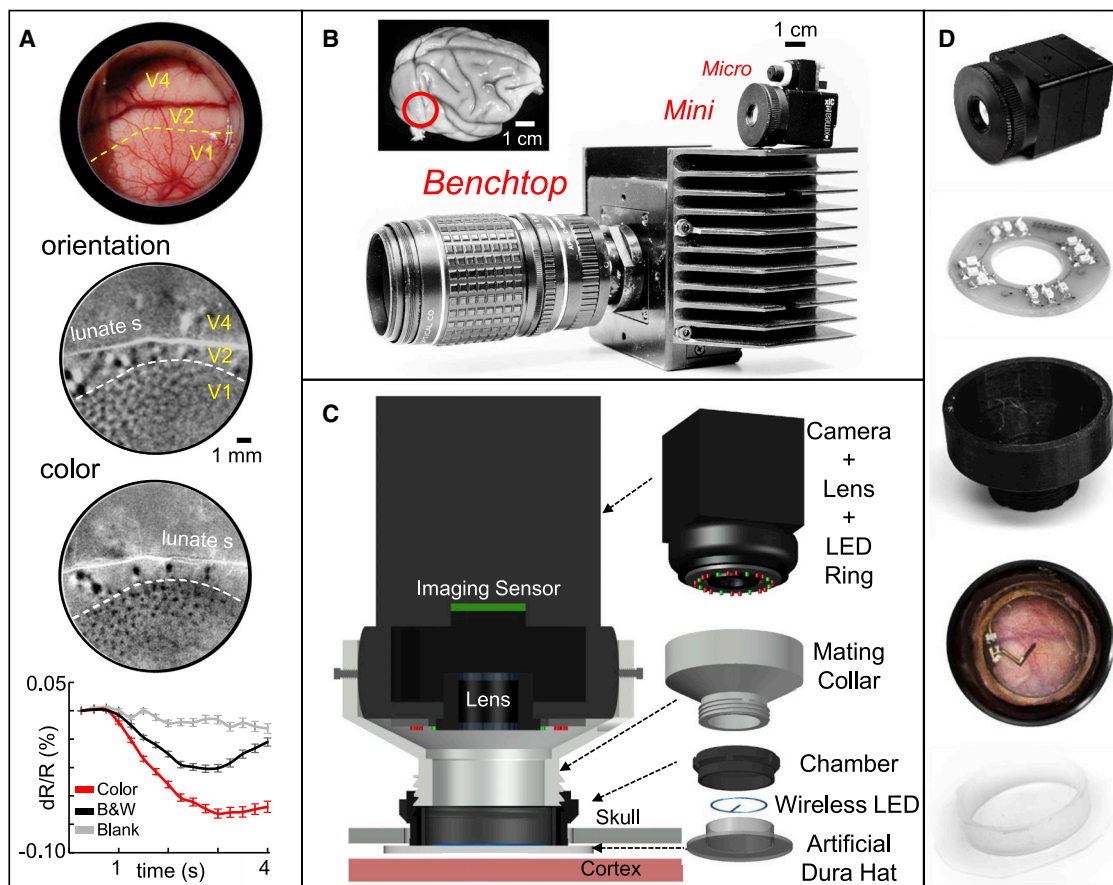
Figure 1. Design of head-mounted camera for optical intrinsic signal imaging

(A) Imaging chamber, optical intrinsic image of orientation and color domains in V1, V2, and V4, and time course of intrinsic signal within V2 color domains to color and achromatic full-screen moving gratings.

(B) Comparison of test cameras with benchtop camera. Inset: location of chamber over a macaque brain.

(C) Exploded diagram of the component parts and cutaway diagram of the assembled multimodal device.

(D) Images of component parts. We chose a Ximea MC023MG-SY as the camera comes in an industry-standard form factor, so it could be replaced with another camera. The code written to collect OISI will support current Ximea or FLIR USB cameras.

multiple brain areas while resolving signal changes comparable to that of benchtop systems. It serves as a first step toward providing an optical capability for studying ethological behavior in macaque monkeys. Preliminary findings of this study have been published in a conference proceeding.[21]

RESULTS

OISI can resolve functional domains of the cerebral cortex. As shown in Figure 1A, OISI over occipital cortex, using a standard benchtop camera (Figure 1B), readily reveals the organization of orientation and color domains in V1, V2, and V4. The orientation map viewed through the optical window shows the response to a 45° grating (dark pixels) minus the response to a 135° grating (bright pixels); the color map shows the response to color (dark pixels) minus achromatic gratings (bright pixels). Because these intrinsic signals are small (0.01%–0.1%), a common approach is to increase the signal-to-noise ratio by averaging across trials and spatial binning. Here, we averaged the responses to 20 stim-

ulus repetitions, binned pixels (1,024 × 1,024 to 512 × 512), and summed images during the period of the hemodynamic response (240 frames at 100 Hz).

Our goal was to produce a head-mounted device (1) composed of readily available components, (2) that would allow for highly focal optogenetic stimulation, and (3) that would provide an FOV large enough to encompass multiple brain areas without the need for head restraint. A maximum weight of 150 g and a height of 8 cm were chosen based on previous NHP head-mounted devices.[22] To enable simultaneous imaging of multiple cortical areas, our system was designed to achieve an FOV of ~100 mm². In addition, we established signal-to-noise requirements capable of detecting small changes in reflectance (~0.01%) and achieving high spatial resolution (~20 μm/pixel) during 5-Hz image acquisition. The hemodynamic signal is slow enough (typically peaking at ~2 s) that 5-Hz data are sufficient to track its temporal dynamics (Figure 1A). Based on our previous experience with intrinsic signal imaging systems, meeting these target specifications would provide a system capable of

Table 1. Comparison of camera specifications for the 3 cameras tested

Camera	Benchtop camera	Mini camera	Micro camera
Make and model	Dalsa 1M60P	XIMEA MC023MG-SY	XIMEA MU9PM-MH
Dimensions (including lens)	150 × 150 × 200 mm, 1.5 kg	30 × 30 × 45 mm, 46.3 g	15 × 15 × 25 mm, 6.6 g
Sensor	Philips FTT1010M	Sony IMX174	Aptina MT9P031
Sensor size, mm	14.34 × 14.34	11.3 × 7.1	5.7 × 4.8
Sensor resolution, pixels	1,024 × 1,024	1,936 × 1,216	2,592 × 1,944
Pixel well depth, K e⁻	180	33	4.9
Pixel percentage change	0.24	0.55	1.43
SNR_{PIX}, dB	52.5	45.2	36.9
Imaging resolution (after spatial binning), pixels	500 × 500	640 × 400	648 × 486
Framerate, fps	100	80	25
Frames per imaging frame (temporal binning)	20	16	5
Imaging frame rate (after binning)	5	5	5
Pixels per superpixel (after spatial binning)	4	9	16
Superpixel well depth, M e⁻	14.4	4.76	0.392
SNR_{MAX} (calculated), dB	71.6	66.8	55.9
No. of imaging frames to 0.01% sensitivity	7	21	255
SNR_{MAX} (measured), dB	63.5	62.4	51.4
Price	∼$40,000 (system: camera, computer, software)	∼$1,600 (camera only)	∼$1,000 (camera only)

Pixel percentage change: the smallest detectable signal as limited by the noise floor of a Poisson distribution ($1/\sqrt{}$(well depth). Imaging resolution: resolution of the camera after pixel binning used for OISI. Superpixel well depth: combined well depth after pixel and frame binning. SNR is typically reported in decibels, so our desired SNR of 10,000 would be expressed as $20 \log_{10}(10,000) = 80$ dB.

mapping cortical functional domains (200–500 μm in diameter) and provide access for targeted optogenetic stimulation of these domains.

Camera selection

We tested two small monochromatic cameras designed for computer vision applications (Figure 1B) against our current benchtop Imager 3001 system (Optical Imaging, Rehovot 76701, Israel) fitted with a Dalsa CCD camera (1M60P, Teledyne DALSA, Waterloo, ON, Canada). This camera will be referred to as the benchtop camera. We chose two different camera/sensor sizes. The larger camera (MC023MG-SY, XIMEA, Münster, Germany) was 30 × 30 × 45 mm and used a Sony IMX174 sensor (referred to as the mini camera). The smallest camera (MU9PM-MH, XIMEA), which has been successfully used for imaging hemodynamic changes during seizure-like activity in rats[14], was 15 × 15 × 25 mm and used an Aptina MT9P031 sensor (referred to as the micro camera). These cameras were selected because they had the highest theoretical ability to detect signal changes (within our camera size and weight criteria) and the desired pixel array size for widefield OISI. Table 1 lists the most relevant specifications for the three cameras.

The size of the signal we typically observe with OISI is between 0.01% and 0.1% change in reflectance.[23,24] However, based on the reported well depth of each sensor, the sensitivity of individual pixels only ranges from 0.24% to 1.43% (Table 1). Consequently, as with the benchtop system, to achieve the signal sensitivity for OISI with these smaller cameras, signal averaging involving temporal and spatial binning and trial averaging is necessary.

We calculated a theoretical maximum signal-to-noise ratio (SNR_{MAX}) after signal averaging[25] for our cameras by deriving a signal-to-noise ratio (SNR) for each pixel based on the reported well depth: SNR of individual pixels (SNR_{PIX}) = $\sqrt{N}$, where N is the number of photons that can be read before a pixel becomes saturated. To optimize illumination conditions for OISI, we illuminate the cortical surface to near-pixel saturation. This makes digital read noise negligible compared with shot noise (defined as the variability in number of photons for a fixed illumination level). Camera digitization was not a factor as all cameras used 12-bit digitization (an ideal detector would have an SNR of 72.25 dB) exceeding the SNR_{PIX} (Table 1). However, the mini and micro cameras record at a higher bit depth than most other head-attached widefield cameras (12 vs. 10 bits), allowing for benchtop levels of signal detection.

To calculate the SNR_{MAX}, we summed well depth across multiple pixels to form superpixels and then summed across frames. To compare the theoretical sensitivity of each camera for OISI, we calculated an SNR_{MAX} based on the assumption that frame binning and pixel binning would capture imaging frames
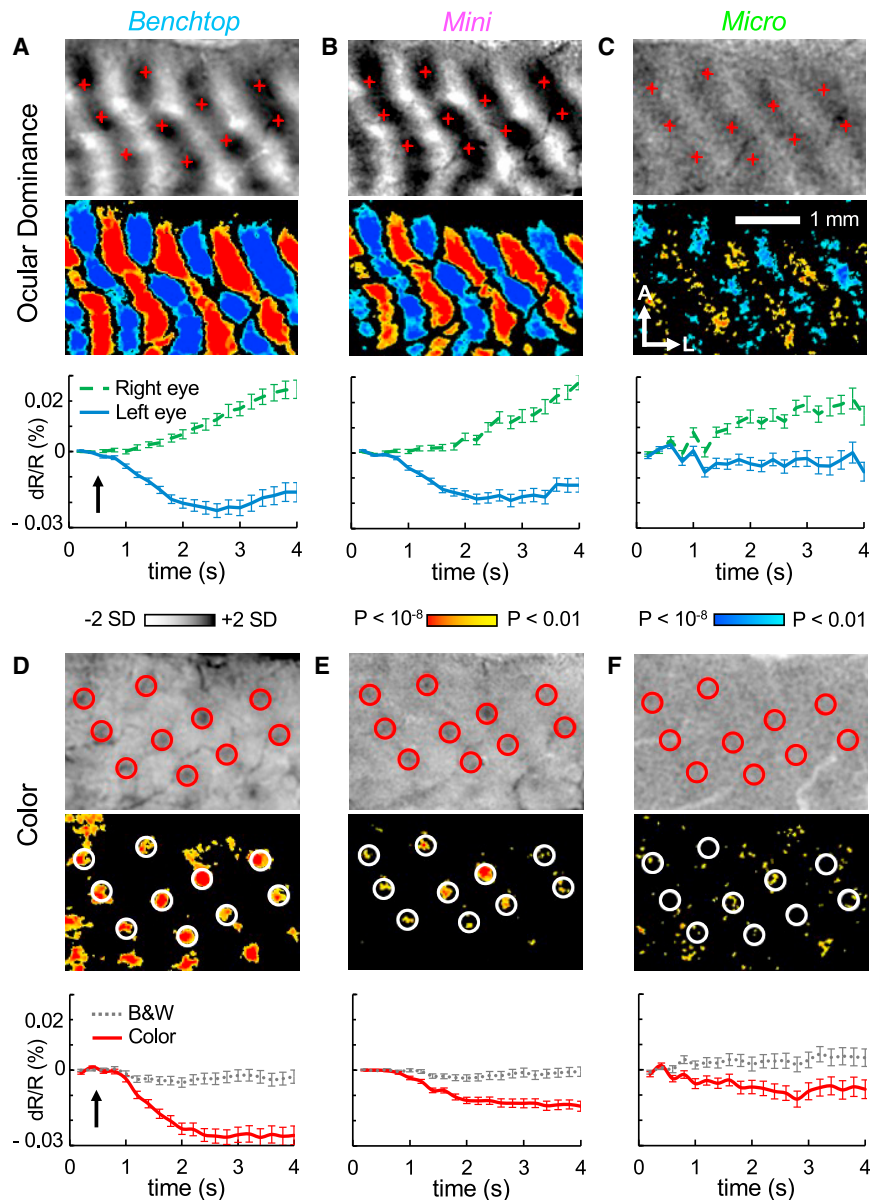
Figure 2. *In vivo* performance of the mini and micro cameras compared with the benchtop camera in the generation of OISI functional maps of macaque visual cortex

(A–C) Benchtop, mini, and micro camera OD OISI maps (top), T-maps (middle), and time courses of response (bottom) in ODCs in V1 to monocular stimulation. Stimulus onset indicated by arrow. (Top row) Maps are a product of summing image frames collected 1.2 to 3.6 s after stimulus onset (frames 8 to 20) from 20 repetitions of each stimulus (0°, 45°, 90°, and 135° full-field moving gratings) presented to one eye minus the summed image frames collected for the other eye. Pixel values are reflectance changes to the left eye, dark stripes, minus response to the right eye, light stripes. Right hemisphere; L, lateral; A, anterior. Images were lowpass filtered at 4 pixels and highpass filtered at 200 pixels. Scale bar: 1 mm. (Middle row) T-maps were generated by pixel-by-pixel Student's t tests showing pixels with significant changes in reflectance for left eye (blue) compared with right eye (red/yellow, p < 0.01). Colored scale bar: $p < 10^{-2}$ to 10^{-8} (uncorrected). (Bottom row) Time courses of the change in reflectance were recorded at regions of interest (ROIs) centered over color blobs (red circles in [D]–[F], top row) and marked by red crosses in the OD maps (top row). Right eye (green) and left eye (blue) lines. Each ROI had an 8-pixel diameter corresponding to an ~200-μm diameter (benchtop camera, 198.4 μm, mini camera, 264.5 μm, micro camera, 203.3 μm). Error bars: SE of mean. Camera comparisons were performed in a single anesthetized experimental session. Cortical illumination was held constant across cameras (instead, exposure time was optimized for each camera). The benchtop and mini cameras revealed ODCs better than the micro camera.

(D–F) Benchtop, mini, and micro camera color OISI maps, T-maps, and time courses of response in color blobs in V1. Same format as (A)–(C). (Top row) Maps are a product of summing image frames from 40 repetitions of 45° and 135° isoluminant red-green gratings minus achromatic gratings presented to the left eye. (Middle row) T-maps show pixels with significant reduction in reflectance for isoluminant color compared with luminant stimuli (red/yellow, p < 0.01). (Bottom row) Time courses of the change in reflectance for the color (red lines) and achromatic (gray lines) stimuli. In contrast to the micro camera, the benchtop and mini cameras detected the color blobs.

approximately 500 pixels wide (the standard imaging resolution used in our lab) at 5 Hz (for a diagram and example of pixel and frame binning, see Figure S1). Finally, to compare the capability of each camera in an experimental setting, we determined the number of imaging frames required to detect a signal change of 0.01%.

To detect a signal change of 0.01%, the SNR_{MAX} of an OISI experiment would need to be 10,000 or greater. This means that $10,000 < \sqrt{N}$, thus N (superpixel well depth) would need to be greater than 100 M e⁻. With these binning parameters, the theoretical superpixel well depth of 14.4 M e⁻ (SNR_{MAX} of 71.6 dB) for the benchtop camera was greater than that of the mini camera (4.76 M e⁻; 66.8 dB) and micro camera (392 K e⁻; 55.9 dB). All 3 cameras still require additional binning to detect a signal change of 0.01% on a frame-by-frame basis at 5 Hz. To reach that, we calculated that the benchtop camera would require binning an additional 7 imaging frames in order to reach the theoretical threshold of 100 M e⁻ for signal detection, while the mini camera would require 21 and the micro camera 255 image frames.

We then experimentally measured the root-mean-square (RMS) signal variance of superpixels (after frame binning and pixel binning) for each camera. The performances of the cameras were roughly in line with the theoretical predictions (SNR_{MAX} [calculated]; Table 1). The mini camera and benchtop camera showed similar SNR_{MAX} (measured) values, with both having more than double the SNR of the micro camera. Based on these SNR estimates and measurements and *in vivo* evaluations (Figure 2), we ultimately chose the Ximea MC023MG-SY mini camera.

Lens selection

Selecting lenses for the mini and micro cameras involved purchasing a series of low-profile, high-definition lenses that were inexpensive, could fit into the designed space, and covered the size of the camera sensors. Lenses are mounted directly to the micro and mini cameras via an anodized aluminum c-mount to an M12 mount adapter. Any M12 mount lens can be mounted; however, to minimize the amount that the device projects above the skull, we placed an ~3-cm ceiling for distance between the camera sensor and the cortical surface. In our design (Figure 1C), the limit that the lens can protrude past the end of the lens mount is ~1.5 cm with a lens diameter restricted to ~1.5 cm or less (~diameter of the recording chamber). As off-the-shelf macro lenses are too large, and lenses with long working distances fall outside of our design constraints, we opted for reversed small standard lenses. Reversed lenses can easily fit, are lightweight, provide short working distances, are cost effective, and provide space for an LED array for cortical illumination. While they have more optical compromises compared with macro lenses, most of these can be largely ignored (except distortion and field curvature), as cortical domains (>100 μm) that we image with widefield OISI do not require anything close to the ~5 μm resolution these cameras could provide with an ideal lens. Issues such as distortion can be easily corrected by generating a standard correction profile from imaging a standard grid or by warping images to a cortical blood vessel map collected with a distortion-free lens.

Since off-the-shelf lenses are not designed or specified for reverse usage, we tested them with the two cameras. Based primarily on FOV considerations, for the mini camera, we selected a 12-mm-focal-length, F/3.0 M12 lens (Sunex DSL901, Sunex, Carlsbad, CA, USA) measuring 13.5 mm in length that provided an FOV of 13.3 × 8.4 mm. For the micro camera, we selected a 7.5-mm F/2.8 M8 lens (Sunex DSL944) measuring 7.5 mm in length that provided a 13.3 × 11.2 mm FOV. FOVs could be adjusted slightly by positioning of the camera and lens. For the benchtop camera, we used a tandem lens combination that provided an FOV of 13.3 × 13.3 mm. Different lenses can be used depending on the desired FOV.

Illumination

Cortical illumination is provided by a ring of eight red (633 nm, 2 × 1.4 mm) and four green (532 nm) surface-mounted LEDs (OSRAM Opto Semiconductors, Regensburg, Germany) on a custom printed circuit board (PCB) attached to the outer rim of the lens (Figures 1C, 1D, and S2). Each LED is individually controlled through software via a 12-channel, 16-bit PWM LED driver (Texas Instruments, Dallas, TX, USA, TLC59711) in an Adafruit breakout board (Adafruit Industries, New York, NY, USA). This allows for more even illumination of the cortical surface.

On-head attachment

Our imaging system is designed to interface (as shown in Figure 1C) directly with a chronically implanted intracranial imaging chamber that is 20 mm in diameter (Figures 1A, chamber walls represented by black circle, and 1C). As shown (Figures 1C and 1D), the mini camera attaches to the chamber via a 3D-printed plastic mating collar. The LED ring used for cortical illumination and lens attach to the camera. Obtaining the desired FOV and focus is achieved by positioning the camera within the camera specific mating collar and locking the camera into place via a set screw. The mating collar is designed to block outside light from entering the FOV, allowing experiments to be conducted without darkening the room. A listing of the components described above and manufacturers can be found in the key resources table.

In vivo cortical functional mapping capability

For *in vivo* testing of the three imaging cameras, we collected OISI from V1 of an anesthetized macaque. We acquired both ocular dominance (OD) and color maps with each camera (Figure 2). Imaging with each camera was performed consecutively in the same experimental procedure with the same lighting (see STAR Methods). These comparisons were chosen because OD is one of the strongest and easiest-to-detect signals to image in V1, while V1 color blobs (V1 cortical domains specific to processing color) have a much smaller physical area and greater selectivity (color), making them more difficult to detect. OD columns (ODCs) are ~400 μm in width and can be centimeters long, while blobs are ~200 μm in diameter.[26]

To examine the *in vivo* SNR capabilities of the three cameras, we compared RMS noise levels during blank stimulus (no visual stimuli presented) trials from the series of OD runs. For the regions of interest (ROIs) shown in Figure 2, the RMS noise level was calculated from the time course data after subtracting the average signal of all the "blank" stimulus trials to remove the

respiratory rhythm from the data. Comparison of RMS noise levels showed *in vivo* SNR (SNR = 1/RMS) camera differences (benchtop camera: 58.1 dB, mini camera: 53.1 dB, and micro camera: 45.4 dB) were proportional to theoretical expectations and *in vitro* measurements (SNR$_{MAX}$; Table 1), suggesting that given the same biological signal, we could expect *in vivo* performance to be proportional to our *in vitro* tests.

To evaluate the capabilities of the cameras to detect functional cortical domains with OISI, OD maps were generated by subtracting changes in cortical reflectance during presentation of stimuli to the left eye from changes during presentation of the same stimuli to the right eye (Figures 2A–2C; see STAR Methods for details on stimuli). The dark stripes in the OD maps (top row) reveal ODCs for the left eye, whereas the light stripes display the ODCs of the right eye. To gauge signal significance in the OISI maps, we generated T-maps (middle row) where pixel-by-pixel Student's t tests were used to identify significant pixels. Pixels with significant response to left-eye stimulation ($p < 0.01$) are shown in blue, while pixels with significant response to right-eye stimulation are shown in yellow/red. To create the color response maps (Figures 2D–2F), changes in cortical reflectance evoked by grayscale luminance stimuli were subtracted from the changes elicited by red/green isoluminant stimuli with the same spatial and temporal frequencies. In the OISI maps (top row), since an increase in neural activity with 630-nm illumination corresponds to a decrease in reflectance, the color blob domains are the dark spots (approximately 200 μm in size). In the T-maps (middle row), pixels with a significant response to color stimuli ($p < 0.01$) are shown in yellow/red.

ODCs were clearly visible using all three cameras, though differences in SNR level were qualitatively (Figures 2A–2C, top row) and quantitatively (T-maps, middle row) evident. V1 color blobs were observed in maps generated by the benchtop and mini cameras (Figures 2D and 2E, top row) as was significant activation within them (middle row); however, images from the micro camera were too noisy for identification of color blobs (Figure 2F). We evaluated OISI signals from 10 ROIs, each ∼200 μm in diameter, that were within left-eye ODCs and centered on color blobs to evaluate the ability of each camera to detect functional hemodynamic response signals over time. For the detection of OD signals, the amplitude and general time course of the intrinsic signals were similar between the benchtop and mini cameras (Figures 2A and 2B, bottom row). The initial decrease in reflectance followed by an increase in response to left-eye stimulation within the left-eye ODCs is typical of an OISI time course with 630-nm illumination.[24,27] In contrast, the time course obtained with the micro camera was much reduced in amplitude (Figure 2C). The detection of color preference at color blob locations also varied between cameras (Figures 2D–2F, bottom row). While the benchtop camera detected a robust change in reflectance, signal amplitudes fell considerably for both the mini and micro cameras. We also examined *in vivo* camera performance based on SNR calculations (Figure S3).

Map stability and consistency between awake and anesthetized states

The goal of our device design is to allow for the stimulation of and recording from distinct functional cortical domains over the

course of training and performance on complex tasks (often taking weeks to years). For this to be feasible, functional domains must be stable over time. Previous studies utilizing OISI have demonstrated the stability in the location of cortical feature domains in the same animal over months to years.[23,28]

We tested whether the chamber-mounted device was capable of reliably imaging cortical functional domains recorded previously. We collected OD and color maps with the mini camera 3 months after using the benchtop camera during chamber implant (Figures 3A–3D). While there were some slight changes in the locations of smaller blood vessels over the course of months (not shown), the locations of functional domains were stable with respect to large blood vessels and other anatomical landmarks. We were able to overlay the OD maps of left-hemisphere V1 taken with the mini camera during awake imaging with those obtained under anesthesia by the benchtop camera (Figures 3B–3D). ODCs aligned up well, although not perfectly. That is because differences in mini camera location and angle with respect to the cortex led to perspective distortions between anatomical landmarks, making complete alignment impossible without image warping. Similarly, in the right hemisphere, color domain maps from V1, V2, and V4 taken under anesthesia with the mini camera could be overlaid directly over those taken by the benchtop camera prior to chamber implant (Figures 3E–3H). The color maps taken weeks apart were nearly perfectly overlapping near any alignment point we chose (based on blood vessel maps). The maps collected by the mini camera (Figures 3C and 3G) were separated by 5 months, supporting the performance and reliability of the mini camera in detecting functional cortical domains.

Wireless μLEDs for optogenetics

To enable stimulation of functional cortical domains, we incorporated a commercially available wireless μLED system (Neurolux, Northfield, IL, USA). The system is designed to wirelessly power μLEDs implanted in rodents via an induction coil wound around the cage.[29] This approach allows for a relatively uniform field strength and ensures robust power delivery. However, due to the size of macaques and the limited power of the antenna, we were unable to readily place an entire monkey within the range of a transmitting antenna coil. Therefore, our approach was to position an antenna above the optical window, over the animal's head, with the wireless μLED located within the field (Figure 4A). With an -antenna 12 cm in diameter, we found that this setup was able to power the wireless μLED as long as the μLED stayed within a range of about 2 cm near the center of the field (Figure S4). Results reported here were with the 12 cm antenna. In subsequent iterations of the antenna design, we found we could increase the antenna size to 30 cm in diameter and place it around an animal's head. This ensured that the μLED was always in range of the antenna during normal NHP head movements for an animal situated in a monkey chair. Designs for different antenna configurations are available in the key resources table.

Potential effects of movement

Allowing animals to move freely dramatically increases the possible types of experiments that can be conducted but also creates the potential for a number of movement-related stability
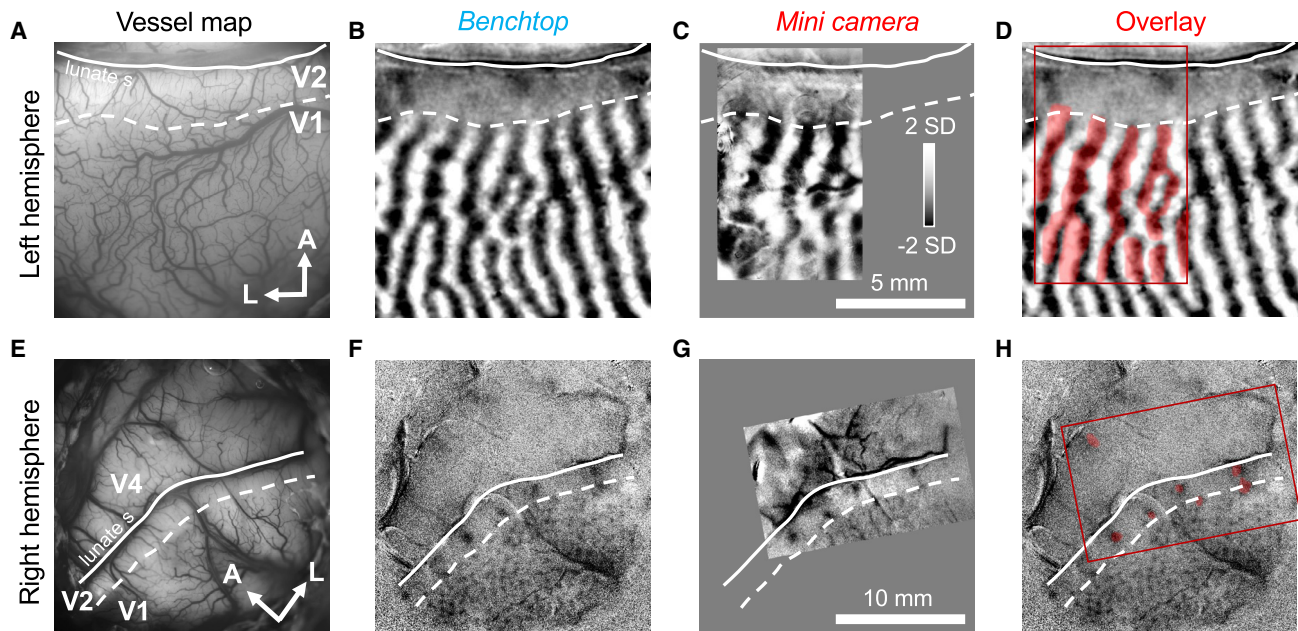
Figure 3. Stability over months of OISI maps of functional domains collected with the benchtop and mini cameras in awake and anesthetized states

(A) Vessel map image of V1 and V2 of the left hemisphere collected under anesthesia using the benchtop camera. A, anterior; L, lateral. Solid white line: lunate sulcus. Dotted white line: V1/V2 border.

(B) ODCs in V1 collected under anesthesia using the benchtop camera.

(C) ODCs imaged 3 months later in the awake monkey with the mini camera attached to the intracranial chamber.

(D) Transparent color overlay (red) of mini camera OD map (C) onto benchtop camera OD map (B). Despite some perspective distortion toward the edge of images due to the mini camera lens's location being much closer to cortical surface than that of the benchtop camera, the ODCs align, although not perfectly.

(E) Vessel map image of V1, V2, and V4 of the right hemisphere collected under anesthesia using the benchtop camera.

(F) Color map imaged under anesthesia with the benchtop camera.

(G) Color map imaged 3 weeks later under anesthesia using the mini camera.

(H) Transparent color overlay of color regions in V2 and V4 collected by the mini camera (G) onto that collected by the benchtop camera (F) show good alignment.

issues in both recording and stimulation. We tested the response of the wireless μLED's output to movement. In Figures 4B and 4C, an accelerometer and light sensor were attached to the μLED and shaken while the μLED was powered on and off by the antenna. The shaking resulted in accelerations (Figure 4B) of up to about $2g$ (equivalent to about 4 times the acceleration experienced by harsh braking in a car)[31] without affecting the μLED's optical output. A plot of μLED output vs. acceleration (Figure 4C) demonstrated reliable performance under conditions harsher than one would expect in a typical experimental setting. In fact, the maximal accelerations of the head of an animal were only about $0.3g$ in the primate chair without head restraint.

Movement artifacts that affect image quality include displacements between the brain, the camera, and the illumination source and are the result of blood pulsation, respiration, and whole-animal movements. Brain-related movements are minimized through stabilizing it via a coverglass and are, subsequently, quite small. To evaluate image stability afforded by the mini camera mounted to the recording chamber in an awake animal, for measures of image stability, we used (1) the number of imaging frames requiring realignment to the first imaging frame (of an image series of 2,000 imaging frames, total of 400 s) and (2) the size of the pixel shift for realignment (Figure 4D). For the mini camera, image stability

was evaluated under free head-movement (blue bars) and head-restrained (red bars) conditions. Image stability was also assessed for the benchtop camera (black bars) positioned above the recording chamber. For the benchtop camera (black bars), imaging frames requiring pixel shifts occurred 10.5 times more frequently (1,474 vs. 140 frames) and were, on average, larger (1.285 vs. 1 pixel) than the mini camera in the head-restrained condition (red bars). Even in the head-movement condition (blue bars), the mini camera exhibited fewer frames that required re-alignment (718 vs. 1,474) than the benchtop camera. In fact, during the head-movement condition with the mini camera, only 5 imaging frames required pixel shifts of greater than 1 pixel; in comparison, the benchtop camera, even with head restraint, required 480 image frames shifts (some of which were as large as 6 pixels). We suspect the primary factor contributing to the improved stability of the mini camera is its direct attachment to the chamber, eliminating movement of the camera relative to the head (a known source of motion-derived noise with the benchtop camera). Figure S5 shows the effect of image frame alignment on OISI image quality.

Optogenetic stimulation with wireless μLEDs

We designed our multimodal device to provide targeted wireless optogenetic stimulation of individual functional domains (see
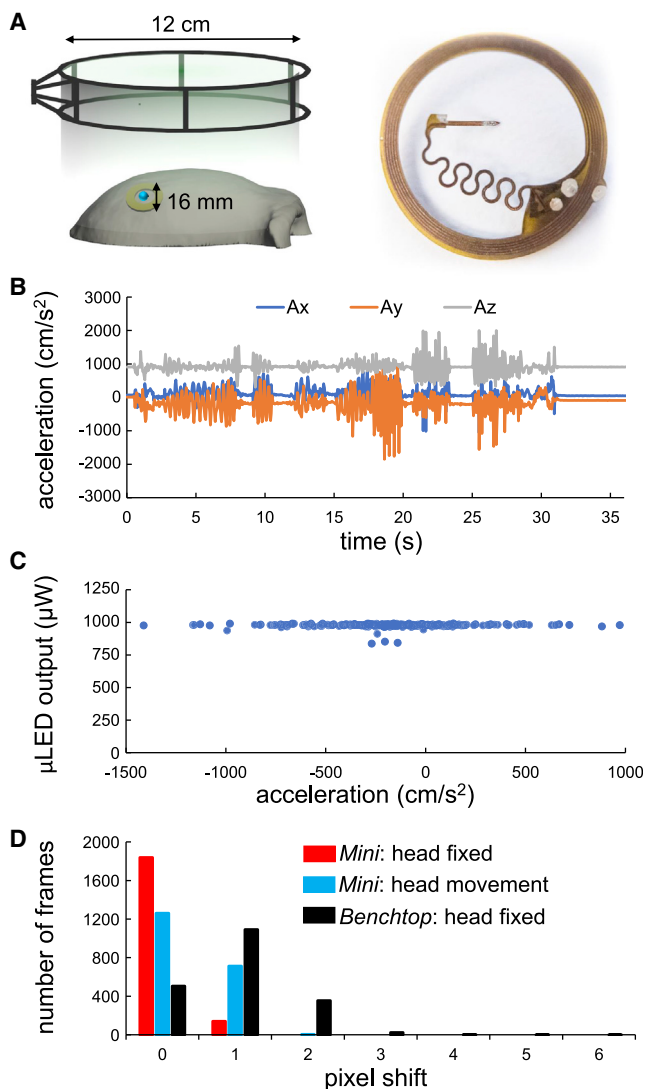
Figure 4. The wireless μLED used for optogenetic stimulation and mini camera perform well when subjected to simulated and animal motion

(A) Diagram of the antenna and wireless μLED, and close-up image of the μLED.

(B and C) Manual shaking of the wireless μLED, powered by the antenna, did not affect the output of light during a 5Hz 50% duty-cycle test.

(B) In a 30 s snippet of shaking, the three traces show data from a triple axis accelerometer attached to the μLED ring. The accelerometer output was digitized at 20 Hz by an Arduino microcontroller.

(C) Measurement of nearly 300 samples (n = 287) of optical output vs. acceleration derived from times when the μLED was flashed on. Output of the μLED was measured via a 1-mm diameter optical fiber coupled to a photodiode. Outliers were not correlated with periods of high acceleration and are likely due to sampling of μLED output during on/off transitions.

(D) The mini camera mounted to the chamber collects fewer imaging frames with movement artifacts than an overhanging benchtop camera. For an ODC imaging run consisting of 2,000 imaging frames (400 s), the histogram shows the number of imaging frames and size of pixel shifts required to align imaging frames collected for the benchtop camera (black) and the mini camera with the animal head restrained (red) or allowing for head movement (blue). Pixel shifts were determined by an image alignment algorithm that shifted image frames

STAR Methods for viral vector injections). After transfection of targeted domains in V2 and V4 (Figure S6), we tested if the wireless μLED implants could evoke an intrinsic response using the head-mounted device with the mini camera in an awake animal. As a first test, we sought to stimulate individual functional domains in V4 as they are larger in size.[23]

We placed the wireless μLED implant on top of the artificial dura hat (see STAR Methods) and directly over a targeted orientation domain in V4 (Figure 5A). In brain tissue, irradiation produced by the μLED remains centered under the μLED and penetrates only a few hundreds of microns (Figure S7). During μLED stimulation, light from the μLED saturates the camera sensor, so imaging is impossible for a few image frames (Figure 5C, horizontal colored bars). With targeted V4 stimulation, neural activation (observed as a local darkening of tissue) was seen in the first frame following the end of stimulation for each stimulus duration (Figure 5C; Video S1). Larger areas of activation (Figure 5B) and increased activation amplitudes (Figures 5C and 5D) were observed (dashed yellow circle) with longer stimulus durations. We also noted possible activation in V2 (dashed blue oval), raising the possibility that at higher intensities inter-areal activation may be achieved. ROI measurements (red cross, Figure 5A) revealed the expected time course of neural activation and confirmed the peak decreases in reflectance were significantly different from no stimulation (Figures 5C and 5D; two tailed t test, p < 0.05). The time course of reflectance change peaked after 2–3 s with amplitudes in the range of 0.01%–0.1% reflectance change, typical for sensory-induced responses and our previous studies using laser coupled fibers for optogenetic stimulation.[18,24] OISI activation centered at the μLED, and not around the receiving coil, supported that neural activation was induced by optogenetic stimulation rather than by indirect effects of the antenna or receiving coil. Electromagnetic waves may affect brain activity by altering the function of calcium channels,[32] but this effect is likely too diffuse to be detected by OISI.

With this setup in an awake, head-restrained monkey with the mini camera, we further tested whether stimulation of one site could lead to activation of a connected site. Figure 6 shows an example of wireless optogenetic stimulation of an orientation domain in area V2 identified in a prior imaging session (Figure 6A). With its small size (220 × 270 × 60 μm) and using a moderate stimulation level (600 ms pulse train, which evoked in V4 a spot of activation of 1–2 mm in size; see Figure 5B), an orientation region in V2 (thick/pale stripe)[33] was activated (Figures 6B and 6C). The time course of response is seen in Figures 6C (red line) and 6B and in Video S2. Wireless μLED stimulation produced a change in reflectance of ∼0.1%–0.15% peaking 1.5–2 s following stimulation onset, typical of intrinsic signals. Initially, in V2, the activation spans roughly 1 mm in size and declines in size after 2 s (Figure 6B). We also observed a significant activation in V1 (Figure 6, blue dot, ROI 2). The stimulated change in reflectance was ∼0.1%–0.15% in magnitude but notably delayed by roughly 2 s in time (Figure 6C). Both the V1 (blue line) and the V2 (red line)

on the x/y plane to the first collected image based on a cross-correlation approach.[30] The ODC image maps collected by the benchtop and mini cameras are shown in Figure S5.
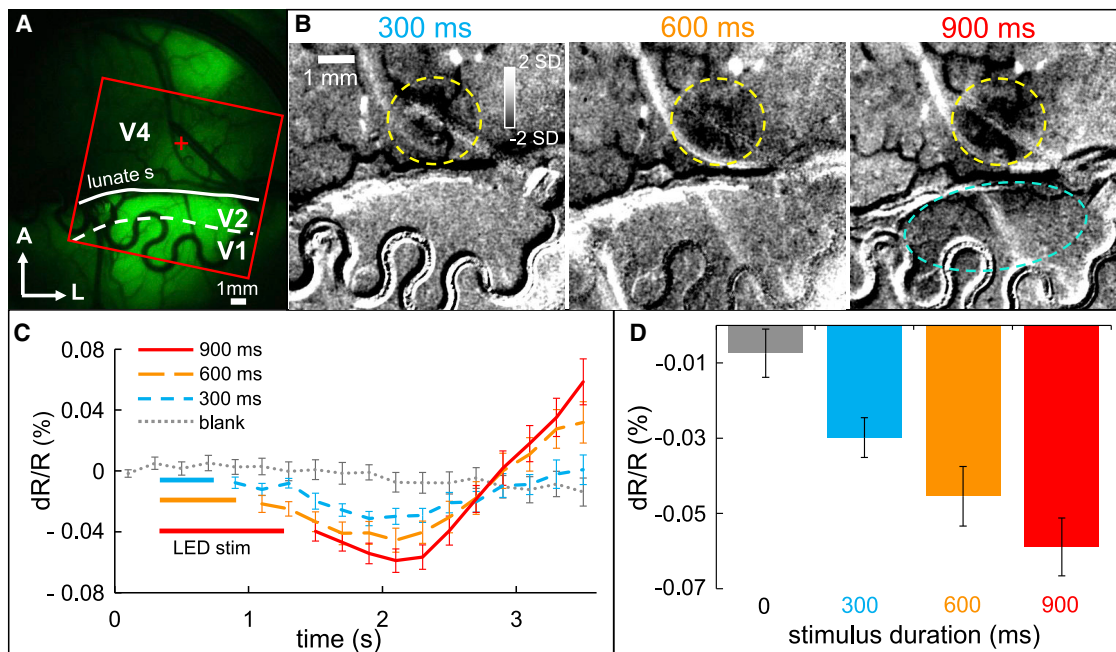
Figure 5. Intrinsic imaging of cortical activation evoked by our head-mounted wireless optogenetic stimulation system

(A) Viral expression (green fluorescence) with approximate location of μLED (red cross) used for optogenetic stimulation. Red box: FOV in (B). A, anterior; L, lateral.

(B) Activation of μLED leads to intrinsic signal response centered on the targeted V4 orientation domain. Images were collected with the mini camera from an awake, head-restrained macaque. Optical stimulation durations: 300, 600, and 900 ms (2 mW, 24 Hz, 20 ms pulse widths). Images summed from 25 trials over frames between 1.8 and 2.2 s after trial onset. Larger areas of activation were observed with longer stimulus durations.

(C) Intrinsic signal response over time at targeted ROI centered at the red cross in (A). ROI: 10-pixel diameter, ~200 μm. Error bars: SEM.

(D) Peak change in reflectance at the ROI for each duration of stimulation. Error bars: SEM. Longer stimulus durations produced larger amplitudes of activation. Stimulation conditions were pseudorandomly interleaved in a block design. Data from 17 trials.

See also Video S1.

time courses were significantly different from no stimulation (Figure 6C, ROI 2: gray line, ROI 1: orange line [two-tailed t test, $p < 0.05$ at 1.6 s for V2, $p < 0.05$ at 3.6 s for V1]). The activation in V1 is consistent with known topographic connectivity between V2 and V1 in both the extent of their feedback and feedforward projections.[34–36] The ~2 s delay is too long for direct activation by the μLED or via direct excitatory connections from V2 to V1. We suspect this activation in V1 is an offset response triggered by the release of inhibition following the end of our stimulation in V2, which needs further exploration.

DISCUSSION

We report the development of a widefield head-mounted intrinsic optical signal imaging and optogenetic stimulation device with the imaging sensitivity of a benchtop optical imaging (OISI) system designed to work with a macaque monkey. The FOV of our device is ~100 times the size of the GRIN lens designs used in primates,[9,10] allowing the simultaneous study of multiple brain regions, which is difficult to achieve with ~1-mm-FOV GRIN-lens-based imaging systems. We demonstrate the system in an awake NHP by imaging functional domains in V1, V2, and V4 and optogenetically stimulating functional domains via wireless μLEDs.

Our device lacks the cellular resolution of 2-photon-based methods, but we posit that the different scales complement each other and the many other modes of recording brain signals, such as single and multiunit electrophysiology, electroencephalogram (EEG), calcium imaging, and fMRI. With a spatial resolution of ~100 μm, an FOV spanning mms to cms, and a temporal resolution of ~80 ms,[24,37] OISI serves to fill the spatiotemporal gap between electrophysiology and fMRI and helps to link responses of individual neurons with mesoscale functional domains and with whole-brain circuits. While there are many studies of neuronal response in awake, behaving primates (mostly head restrained), there is a lack of understanding of how populations of neurons (columns, domains) behave at mesoscale within and across cortical areas. Our head-mounted multimodal approach offers an avenue for studying the role of the functional organizations of multiple areas that can ultimately link our multiscale and multimodal understanding of the neural circuits underlying behavior.[38,39]

While it allows for head movements, the device is designed for use on an animal in a primate chair. Even with this limitation, the capability of studying an NHP with the ability to move their head in conjunction with their eyes could reveal dramatic behavioral and neural processing differences compared with animals that are head fixed.[40,41] Furthermore, allowing for head movement would lead to greater animal comfort in a primate chair and could
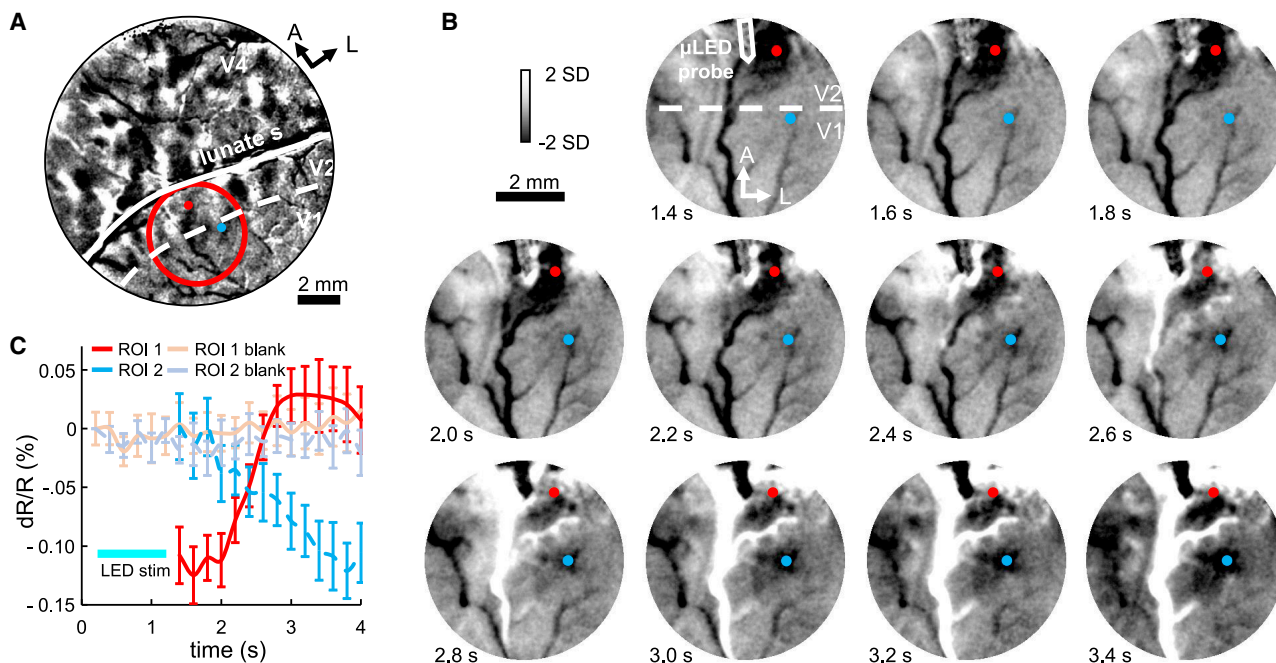
Figure 6. Optogenetic stimulation of orientation domain in V2 leads to activation of domains in V1

(A) Orientation map (45° vs. 135°) collected previously under anesthesia in V1, V2, and V4. Red circle: location of FOV in (B). Red dot (ROI 1): location of stimulation in area V2. Blue dot (ROI 2): location of delayed activation in area V1 (B and C). A, anterior; L, lateral.

(B) Images of V1 and V2 following stimulation of an orientation domain in area V2. Stimulation and image collection were accomplished with the head-mounted device in an awake, head-restrained macaque. Stimulation: 600-ms duration pulse train (2 mW, 24 Hz, pulse width 20 ms). Images are first-frame subtracted. Red dot (ROI 1): location of stimulation in area V2. Blue dot (ROI 2): location of delayed activation in area V1. Average of 11 trials.

(C) Intrinsic signal response over time with μLED stimulation in V2 (ROI 1 red dot, red curve) and V1 (ROI 2, blue dot, blue curve). Each ROI: 5 pixels (~100 μm) in diameter. Due to saturation by μLED, no hemodynamic response is registered during stimulation (cyan bar). Gray (ROI 2) and orange (ROI 1) colored lines from the same ROI locations show responses during no stimulation trials and serve as controls in lieu of presenting additional time courses from control ROI locations. Error bars: SEM.

See also Video S2.

accelerate learning of tasks and reduce the level of food and water reinforcement but could also have important implications when studies are concerned with stress-related hormonal and neurotransmitter systems.[42–44]

Studies using neuroimaging and optogenetic stimulation of freely moving small animals have dramatically expanded the types of experiments being performed to increase our understanding of behavior and the brain.[45–47] Optogenetics is showing a similar promise to probe primate brain circuitry.[48–55] However, there are few neuroimaging and optogenetic studies of primates in more ethological and less physically restricted behaviors.[9,10] We hope that our multimodal approach can open the door to the study of more natural and social primate behaviors like grooming, sleeping, and ambulating.[10,56]

Limitations of the study

We can envision further improvements of our system. First, it can be made fully wireless[57–60] rather than being tethered, thereby providing the potential of studying NHP behavior in more natural environments. This would require the addition of a battery, which could potentially power both the camera and LED illumination and the μLEDs for optogenetic stimulation,[61] an onboard microcomputer for image processing, and some

form of data storage. Second, individual control of different wavelength μLEDs or an array of μLEDs[62,63] would expand optogenetic stimulation as well as imaging capabilities. It is possible to make μLEDs almost invisible by using transparent materials,[64,65] allowing for imaging of the stimulated areas and not just their surroundings. We designed the chamber-mounted imaging system specifically for OISI; however, it could be adapted for other modalities. Methods such as electrophysiology or fluorescence can be incorporated. Widefield imaging of fluorescent signals could be achieved by adding blue illumination LEDs and a relevant filter set. In the case of fluorescent imaging without OISI, the dark-noise performance of a camera would be an important selection criterion, and a smaller camera like the micro camera might suffice.

STAR★METHODS

Detailed methods are provided in the online version of this paper and include the following:

- KEY RESOURCES TABLE
- RESOURCE AVAILABILITY
    - ○ Lead contact

Cell Reports Methods
Article

REFERENCES

1. Sawinski, J., Wallace, D.J., Greenberg, D.S., Grossmann, S., Denk, W., and Kerr, J.N.D. (2009). Visually evoked activity in cortical cells imaged in freely moving animals. Proc. Natl. Acad. Sci. USA 106, 19557–19562. https://doi.org/10.1073/pnas.0903680106.

2. Kitamura, T., Ogawa, S.K., Roy, D.S., Okuyama, T., Morrissey, M.D., Smith, L.M., Redondo, R.L., and Tonegawa, S. (2017). Engrams and circuits crucial for systems consolidation of a memory. Science 356, 73–78. https://doi.org/10.1126/science.aam6808.

3. Liberti, W.A., Perkins, L.N., Leman, D.P., and Gardner, T.J. (2017). An open source, wireless capable miniature microscope system. J. Neural. Eng. 14, 045001. https://doi.org/10.1088/1741-2552/aa6806.

4. Roberts, T.F., Hisey, E., Tanaka, M., Kearney, M.G., Chattree, G., Yang, C.F., Shah, N.M., and Mooney, R. (2017). Identification of a motor-to-auditory pathway important for vocal learning. Nat. Neurosci. 20, 978–986. https://doi.org/10.1038/nn.4563.

5. Kinsky, N.R., Sullivan, D.W., Mau, W., Hasselmo, M.E., and Eichenbaum, H.B. (2018). Hippocampal place fields maintain a coherent and flexible map across long timescales. Curr. Biol. 28, 3578–3588.e6. https://doi.org/10.1016/j.cub.2018.09.037.

6. Ju, N., Jiang, R., Macknik, S.L., Martinez-Conde, S., and Tang, S. (2018). Long-term all-optical interrogation of cortical neurons in awake-behaving nonhuman primates. PLoS Biol. 16, e2005839. https://doi.org/10.1371/journal.pbio.2005839.

7. Bollimunta, A., Santacruz, S.R., Eaton, R.W., Xu, P.S., Morrison, J.H., Moxon, K.A., Carmena, J.M., and Nassi, J.J. (2011). Head-mounted microendoscopic calcium imaging in dorsal premotor cortex of behaving rhesus macaque. Cell Rep. 35, 109239. https://doi.org/10.1016/j.celrep.2021.109239.

8. Seidemann, E., Chen, Y., Bai, Y., Chen, S.C., Mehta, P., Kajs, B.L., Geisler, W.S., and Zemelman, B.V. (2016). Calcium imaging with genetically encoded indicators in behaving primates. Elife 5, e16178. https://doi.org/10.7554/eLife.16178.

9. Ebina, T., Masamizu, Y., Tanaka, Y.R., Watakabe, A., Hirakawa, R., Hirayama, Y., Hira, R., Terada, S.I., Koketsu, D., Hikosaka, K., and Matsuzaki, M. (2018). Two-photon imaging of neuronal activity in motor cortex of marmosets during upper-limb movement tasks. Nat. Commun. 9, 1879. https://doi.org/10.1038/s41467-018-04286-6.

10. Kondo, T., Saito, R., Otaka, M., Yoshino-Saito, K., Yamanaka, A., Yamamori, T., Watakabe, A., Mizukami, H., Schnitzer, M.J., Tanaka, K.F., et al. (2018). Calcium transient dynamics of neural ensembles in the primary motor cortex of naturally behaving monkeys. Cell Rep. 24, 2191–2195.e4. https://doi.org/10.1016/j.celrep.2018.07.057.

11. Ju, N.S., Guan, S.C., Tao, L., Tang, S.M., and Yu, C. (2021). Orientation tuning and end-stopping in macaque V1 studied with two-photon calcium imaging. Cereb. Cortex 31, 2085–2097. https://doi.org/10.1093/cercor/bhaa346.

12. Ferezou, I., Bolea, S., and Petersen, C.C.H. (2006). Visualizing the cortical representation of whisker touch: voltage-sensitive dye imaging in freely moving mice. Neuron 50, 617–629. https://doi.org/10.1016/j.neuron.2006.03.043.

13. Miao, P., Zhang, L., Li, M., Zhang, Y., Feng, S., Wang, Q., and Thakor, N.V. (2017). Chronic wide-field imaging of brain hemodynamics in behaving animals. Biomed. Opt Express 8, 436–445. https://doi.org/10.1364/BOE.8.000436.

14. Sigal, I., Koletar, M.M., Ringuette, D., Gad, R., Jeffrey, M., Carlen, P.L., Stefanovic, B., and Levi, O. (2016). Imaging brain activity during seizures in freely behaving rats using a miniature multi-modal imaging system. Biomed. Opt Express 7, 3596–3609. https://doi.org/10.1364/BOE.7.003596.

15. Senarathna, J., Yu, H., Deng, C., Zou, A.L., Issa, J.B., Hadjiabadi, D.H., Gil, S., Wang, Q., Tyler, B.M., Thakor, N.V., and Pathak, A.P. (2019). A miniature multi-contrast microscope for functional imaging in freely behaving animals. Nat. Commun. 10, 99. https://doi.org/10.1038/s41467-018-07926-z.

16. Scott, B.B., Thiberge, S.Y., Guo, C., Tervo, D.G.R., Brody, C.D., Karpova, A.Y., and Tank, D.W. (2018). Imaging cortical dynamics in GCaMP transgenic rats with a head-mounted widefield macroscope. Neuron 100, 1045–1058. https://doi.org/10.1016/j.neuron.2018.09.050.

17. Roe, A.W., Chernov, M.M., Friedman, R.M., and Chen, G. (2015). In vivo mapping of cortical columnar networks in the monkey with focal electrical and optical stimulation. Front. Neuroanat. 9, 135. https://doi.org/10.3389/fnana.2015.00135.

18. Chernov, M.M., Friedman, R.M., Chen, G., Stoner, G.R., and Roe, A.W. (2018). Functionally specific optogenetic modulation in primate visual cortex. Proc. Natl. Acad. Sci. USA 115, 10505–10510. https://doi.org/10.1073/pnas.1802018115.

19. Chernov, M.M., Friedman, R.M., Zaraza, D., and Roe, A.W. (2018). Activation of Functional Domains in the Primate Cortex with Infrared Neural Stimulation (SPIE Photonics West, San Francisco, CA).

20. Nakamichi, Y., Okubo, K., Sato, T., Hashimoto, M., and Tanifuji, M. (2019). Optical intrinsic signal imaging with optogenetics reveals functional

cortico-cortical connectivity at the columnar level in living macaques. Sci. Rep. *9*, 6466. https://doi.org/10.1038/s41598-019-42923-2.

21. Zaraza, D., Chernov, M., Friedman, R.M., Yang, Y., Rogers, J.A., and Roe, A.W. (2020). Going wireless: an optical imaging and optogenetics system for use in awake behaving primates. Optogenetics and Optical Manipulation 2020, 11227. International Society for Optics and Photonics. https://doi.org/10.1117/12.2546289.

22. Gilja, V., Chestek, C.A., Nuyujukian, P., Foster, J., and Shenoy, K.V. (2010). Autonomous head-mounted electrophysiology systems for freely behaving primates. Curr. Opin. Neurobiol. *20*, 676–686. https://doi.org/10.1016/j.conb.2010.06.007.

23. Tanigawa, H., Lu, H.D., and Roe, A.W. (2010). Functional organization for color and orientation in macaque V4. Nat. Neurosci. *13*, 1542–1548. https://doi.org/10.1038/nn.2676.

24. Lu, H.D., Chen, G., Cai, J., and Roe, A.W. (2017). Intrinsic signal optical imaging of visual brain activity: tracking of fast cortical dynamics. Neuroimage *148*, 160–168. https://doi.org/10.1016/j.neuroimage.2017.01.006.

25. Van Drongelen, W. (2007). Signal averaging. In Signal Processing for Neuroscientists introduction to the Analysis of Physiological Signals, W. van Drongelen, ed. (Academic Press), pp. 55–70. https://doi.org/10.1016/B978-012370867-0/50004-8.

26. Lu, H.D., and Roe, A.W. (2008). Functional organization of color domains in V1 and V2 of macaque monkey revealed by optical imaging. Cereb. Cortex *18*, 516–533. https://doi.org/10.1093/cercor/bhm081.

27. Bonhoeffer, T., and Grinvald, A. (1996). Optical imaging based on intrinsic signals: the methodology. In Brain Mapping: The Methods, A.W. Toga and J.C. Mazziotta, eds. (Academic Press), pp. 97–137.

28. Chen, L.M., Heider, B., Williams, G.V., Healy, F.L., Ramsden, B.M., and Roe, A.W. (2002). A chamber and artificial dura method for long-term optical imaging in the monkey. J. Neurosci. Methods *113*, 41–49. https://doi.org/10.1016/s0165-0270(01)00475-7.

29. Shin, G., Gomez, A.M., Al-Hasani, R., Jeong, Y.R., Kim, J., Xie, Z., Banks, A., Lee, S.M., Han, S.Y., Yoo, C.J., et al. (2017). Flexible near-field wireless optoelectronics as subdermal implants for broad applications in optogenetics. Neuron *93*, 509–521.e3. https://doi.org/10.1016/j.neuron.2016.12.031.

30. Roe, A.W. (2007). Long-term optical imaging of intrinsic signals in anesthetized and awake monkeys. Appl. Opt. *46*, 1872–1880.

31. Bokare, P.S., and Maurya, A.K. (2017). Acceleration-deceleration behaviour of various vehicle types. Transport. Res. Procedia *25*, 4733–4749. https://doi.org/10.1016/j.trpro.2017.05.486.

32. Pall, M.L. (2013). Electromagnetic fields act via activation of voltage-gated calcium channels to produce beneficial or adverse effects. J. Cell Mol. Med. *17*, 958–965. https://doi.org/10.1111/jcmm.12088.

33. Roe, A.W., and Ts'o, D.Y. (1995). Visual topography in primate V2: multiple representation across functional stripes. J. Neurosci. *15*, 3689–3715. https://doi.org/10.1523/JNEUROSCI.15-05-03689.

34. Livingstone, M.S., and Hubel, D.H. (1984). Anatomy and physiology of a color system in the primate visual cortex. J. Neurosci. *4*, 309–356. https://doi.org/10.1523/JNEUROSCI.04-01-00309.1984.

35. Shmuel, A., Korman, M., Sterkin, A., Harel, M., Ullman, S., Malach, R., and Grinvald, A. (2005). Retinotopic axis specificity and selective clustering of feedback projections from V2 to V1 in the owl monkey. J. Neurosci. *25*, 2117–2131. https://doi.org/10.1523/JNEUROSCI.4137-04.2005.

36. Federer, F., Ichida, J.M., Jeffs, J., Schiessl, I., McLoughlin, N., and Angelucci, A. (2009). Four projection streams from primate V1 to the cytochrome oxidase stripes of V2. J. Neurosci. *29*, 15455–15471. https://doi.org/10.1523/JNEUROSCI.1648-09.2009.

37. Pouratian, N., and Toga, A.W. (2002). Optical imaging based on intrinsic signals. In Brain Mapping: The Methods, A.W. Toga and J.C. Mazziotta, eds. (Academic Press), pp. 97–140. https://doi.org/10.1016/B978-012693019-1/50007-1.

38. Nassi, J.J., Avery, M.C., Cetin, A.H., Roe, A.W., and Reynolds, J.H. (2015). Optogenetic activation of normalization in alert macaque visual cortex. Neuron *86*, 1504–1517. https://doi.org/10.1016/j.neuron.2015.05.040.

39. Roe, A.W. (2019). Columnar connectome: toward a mathematics of brain function. Netw. Neurosci. *3*, 779–791. https://doi.org/10.1162/netn_a_00088.

40. McCluskey, M.K., and Cullen, K.E. (2007). Eye, head, and body coordination during large gaze shifts in rhesus monkeys: movement kinematics and the influence of posture. J. Neurophysiol. *97*, 2976–2991. https://doi.org/10.1152/jn.00822.2006.

41. King, W.M., and Shanidze, N. (2011). Anticipatory eye movements stabilize gaze during self-generated head movements. Ann. N. Y. Acad. Sci. *1233*, 219–225. https://doi.org/10.1111/j.1749-6632.2011.06165.x.

42. Calapai, A., Berger, M., Niessing, M., Heisig, K., Brockhausen, R., Treue, S., and Gail, A. (2017). A cage-based training, cognitive testing and enrichment system optimized for rhesus macaques in neuroscience research. Behav. Res. Methods *49*, 35–45. https://doi.org/10.3758/s13428-016-0707-3.

43. Shnitko, T.A., Allen, D.C., Gonzales, S.W., Walter, N.A., and Grant, K.A. (2017). Ranking cognitive flexibility in a group setting of rhesus monkeys with a set-shifting procedure. Front. Behav. Neurosci. *11*, 55. https://doi.org/10.3389/fnbeh.2017.00055.

44. Pfefferle, D., Plümer, S., Burchardt, L., Treue, S., and Gail, A. (2018). Assessment of stress responses in rhesus macaques (Macaca mulatta) to daily routine procedures in system neuroscience based on salivary cortisol concentrations. PLoS One *13*, e0190190. https://doi.org/10.1371/journal.pone.0190190.

45. Jimenez, J.C., Su, K., Goldberg, A.R., Luna, V.M., Biane, J.S., Ordek, G., Zhou, P., Ong, S.K., Wright, M.A., Zweifel, L., and Kheirbek, M.A. (2018). Anxiety cells in a hippocampal-hypothalamic circuit. Neuron *97*, 670–683.e6. https://doi.org/10.1016/j.neuron.2018.01.016.

46. Adam, Y., Kim, J.J., Lou, S., Zhao, Y., Xie, M.E., Brinks, D., Wu, H., Mostajo-Radji, M.A., Kheifets, S., Parot, V., et al. (2019). Voltage imaging and optogenetics reveal behaviour-dependent changes in hippocampal dynamics. Nature *569*, 413–417. https://doi.org/10.1038/s41586-019-1166-7.

47. Kumar, D., Koyanagi, I., Carrier-Ruiz, A., Vergara, P., Srinivasan, S., Sugaya, Y., Kasuya, M., Yu, T.S., Vogt, K.E., Muratani, M., et al. (2020). Sparse activity of hippocampal adult-born neurons during REM sleep is necessary for memory consolidation. Neuron *107*, 552–565.e10. https://doi.org/10.1016/j.neuron.2020.05.008.

48. Gerits, A., Farivar, R., Rosen, B.R., Wald, L.L., Boyden, E.S., and Vanduffel, W. (2012). Optogenetically induced behavioral and functional network changes in primates. Curr. Biol. *22*, 1722–1726. https://doi.org/10.1016/j.cub.2012.07.023.

49. May, T., Ozden, I., Brush, B., Borton, D., Wagner, F., Agha, N., Sheinberg, D.L., and Nurmikko, A.V. (2014). Detection of optogenetic stimulation in somatosensory cortex by non-human primates-towards artificial tactile sensation. PLoS One *9*, e114529. https://doi.org/10.1371/journal.pone.0114529.

50. Acker, L., Pino, E.N., Boyden, E.S., and Desimone, R. (2016). FEF inactivation with improved optogenetic methods. Proc. Natl. Acad. Sci. USA *113*, E7297–E7306. https://doi.org/10.1073/pnas.1610784113.

51. Yazdan-Shahmorad, A., Diaz-Botia, C., Hanson, T.L., Kharazia, V., Ledochowitsch, P., Maharbiz, M.M., and Sabes, P.N. (2016). A large-scale interface for optogenetic stimulation and recording in nonhuman primates. Neuron *89*, 927–939. https://doi.org/10.1016/j.neuron.2016.01.013.

52. Galvan, A., Stauffer, W.R., Acker, L., El-Shamayleh, Y., Inoue, K.I., Ohayon, S., and Schmid, M.C. (2017). Nonhuman primate optogenetics: recent advances and future directions. J. Neurosci. *37*, 10894–10903. https://doi.org/10.1523/JNEUROSCI.1839-17.2017.

53. Andrei, A.R., Pojoga, S., Janz, R., and Dragoi, V. (2019). Integration of cortical population signals for visual perception. Nat. Commun. *10*, 3832. https://doi.org/10.1038/s41467-019-11736-2.

54. De, A., El-Shamayleh, Y., and Horwitz, G.D. (2020). Fast and reversible neural inactivation in macaque cortex by optogenetic stimulation of GABAergic neurons. Elife *9*, e52658. https://doi.org/10.7554/eLife.52658.

55. Tremblay, S., Acker, L., Afraz, A., Albaugh, D.L., Amita, H., Andrei, A.R., Angelucci, A., Aschner, A., Balan, P.F., Basso, M.A., et al. (2020). An open resource for non-human primate optogenetics. Neuron *108*, 1075–1090.e6. https://doi.org/10.1016/j.neuron.2020.09.027.

56. Yu, H., Senarathna, J., Tyler, B.M., Thakor, N.V., and Pathak, A.P. (2015). Miniaturized optical neuroimaging in unrestrained animals. Neuroimage *113*, 397–406. https://doi.org/10.1016/j.neuroimage.2015.02.070.

57. Won, S.M., Cai, L., Gutruf, P., and Rogers, J.A. (2021). Wireless and battery-free technologies for neuroengineering. Nat. Biomed. Eng., 1–19. https://doi.org/10.1038/s41551-021-00683-3.

58. Hampson, R.E., Collins, V., and Deadwyler, S.A. (2009). A wireless recording system that utilizes Bluetooth technology to transmit neural activity in freely moving animals. J. Neurosci. Methods *182*, 195–204. https://doi.org/10.1016/j.jneumeth.2009.06.007.

59. Lo, Y.K., Kuan, Y.C., Culaclii, S., Kim, B., Wang, P.M., Chang, C.W., Massachi, J.A., Chen, K., Gad, P., et al. (2017). Fully integrated wireless SoC for motor function recovery after spinal cord injury. IEEE Trans. Biomed. Circuits Syst. *11*, 497–509. https://doi.org/10.1109/TBCAS.2017.2679441.

60. Ramshur, J.T., Morshed, B.I., de Jongh Curry, A.L., and Waters, R.S. (2019). Telemetry-controlled simultaneous stimulation-and-recording device (SRD) to study interhemispheric cortical circuits in rat primary somatosensory (SI) cortex. BMC Biomed. Eng. *8*, 1–19. https://doi.org/10.1186/s42490-019-0019-7.

61. Dagnew, R., Lin, Y.Y., Agatep, J., Cheng, M., Jann, A., Quach, V., and Walwyn, W. (2017). CerebraLux: a low-cost, open-source, wireless probe for optogenetic stimulation. Neurophotonics *4*, 045001. https://doi.org/10.1117/1.NPh.4.4.045001.

62. Mayer, P., Sivakumar, N., Pritz, M., Varga, M., Mehmann, A., Lee, S., Salvatore, A., Magno, M., Pharr, M., Johannssen, H.C., et al. (2019). Flexible and lightweight devices for wireless multi-color optogenetic experiments controllable via commercial cell phones. Front. Neurosci. *13*, 819. https://doi.org/10.3389/fnins.2019.00819.

63. Ausra, J., Wu, M., Zhang, X., Vázquez-Guardado, A., Skelton, P., Peralta, R., Avila, R., Murickan, T., Haney, C.R., Huang, Y., et al. (2021). Wireless, battery-free, subdermally implantable platforms for transcranial and long-range optogenetics in freely moving animals. Proc. Natl. Acad. Sci. USA *118*, e2025775118. https://doi.org/10.1073/pnas.2025775118.

64. Kim, R.H., Bae, M.H., Kim, D.G., Cheng, H., Kim, B.H., Kim, D.H., Wu, J., Du, F., Kim, H.S., Kim, S., et al. (2011). Stretchable, transparent graphene interconnects for arrays of microscale inorganic light emitting diodes on rubber substrates. Nano Lett. *11*, 3881–3886. https://doi.org/10.1021/nl202000u.

65. Brosch, M., Deckert, M., Rathi, S., Takagaki, K., Weidner, T., Ohl, F.W., Schmidt, B., and Lippert, M.T. (2020). An optically transparent multi-electrode array for combined electrophysiology and optophysiology at the mesoscopic scale. J. Neural. Eng. *17*, 046014. https://doi.org/10.1088/1741-2552/aba1a4.

66. Lee, J.H., Durand, R., Gradinaru, V., Zhang, F., Goshen, I., Kim, D.S., Fenno, L.E., Ramakrishnan, C., and Deisseroth, K. (2010). Global and local fMRI signals driven by neurons defined optogenetically by type and wiring. Nature *465*, 788–792. https://doi.org/10.1038/nature09108.

67. Ruiz, O., Lustig, B.R., Nassi, J.J., Cetin, A., Reynolds, J.H., Albright, T.D., Callaway, E.M., Stoner, G.R., and Roe, A.W. (2013). Optogenetics through windows on the brain in the nonhuman primate. J. Neurophysiol. *110*, 1455–1467. https://doi.org/10.1152/jn.00153.2013.

68. McAlinden, N., Massoubre, D., Richardson, E., Gu, E., Sakata, S., Dawson, M.D., and Mathieson, K. (2013). Thermal and optical characterization of micro-LED probes for in vivo optogenetic neural stimulation. Opt. Lett. *38*, 992–994. https://doi.org/10.1364/OL.38.000992.

69. Klapoetke, N.C., Murata, Y., Kim, S.S., Pulver, S.R., Birdsey-Benson, A., Cho, Y.K., Morimoto, T.K., Chuong, A.S., Carpenter, E.J., Tian, Z., et al. (2014). Independent optical excitation of distinct neural populations. Nat. Methods *11*, 338–346. https://doi.org/10.1038/nmeth.2836.

STAR★METHODS

KEY RESOURCES TABLE

REAGENT or RESOURCE	SOURCE	IDENTIFIER
Bacterial and virus strains		
AAV5-CaMkII-hChR2(H134R)-EYFP	Lee et al.[66]	Addgene plasmid # 26969-AAV5; RRID:Addgene_26969
AAV9-CaMkII-hChR2(H134R)-EYFP	Lee et al.[66]	Addgene plasmid # 26969-AAV9; RRID:Addgene_26969
Experimental models: Organisms/Strains		
Rhesus macaque	Oregon National Primate Research Center	*Macaca mulatta*
Software and algorithms		
Camera acquisition software	This paper	https://doi.org/10.5281/zenodo.7246080
XIMEA CamTool	XIMEA GmbH, Münster, Germany	https://www.ximea.com/support/wiki/allprod/XIMEA_CamTool
Illumination control software	This paper	https://github.com/IntrinsicOpticalImaging/miniOISI/blob/main/LED_control_individual.ino
Other		
Hardware and assembly instructions	This paper	https://github.com/IntrinsicOpticalImaging/miniOISI/tree/main#readme
LED illumination ring for OISI	This paper	https://github.com/IntrinsicOpticalImaging/miniOISI/blob/main/LED_ring.rrb
3D printable design for camera holder	This paper	https://github.com/IntrinsicOpticalImaging/miniOISI/blob/main/camera_sheath.stl
3D printable design for camera mating collar	This paper	https://github.com/IntrinsicOpticalImaging/miniOISI/blob/main/CameraToChamber.stl
3D printable design for intracranial chamber	This paper	https://github.com/IntrinsicOpticalImaging/miniOISI/blob/main/small_lip_chamber.stl
3D printable design for 140 mm antenna	This paper	https://github.com/IntrinsicOpticalImaging/miniOISI/blob/main/Antenna_140mm.stl
3D printable design for 230 mm antenna	This paper	https://github.com/IntrinsicOpticalImaging/miniOISI/tree/main/antenna_230mm
3D printable design for 300 mm antenna	This paper	https://github.com/IntrinsicOpticalImaging/miniOISI/tree/main/antenna_300mm
Mini camera (XIMEA MC023MG-SY)	XIMEA GmbH, Münster, Germany	https://www.ximea.com/en/products/usb-31-gen-1-with-sony-cmos-xic/mc023mg-sy
Micro camera (XIMEA MU9PM-MH)	XIMEA GmbH, Münster, Germany	https://www.ximea.com/en/products/application-specific-cameras/subminiature-cameras/mu9pm-mh
Lens mount adapter (Basler, 2000035953)	Basler AG, Ahrensburg, Germany	https://www.baslerweb.com/en/products/vision-components/accessories-and-bundles/cs-mount-to-s-mount-adapter/

Continued

REAGENT or RESOURCE	SOURCE	IDENTIFIER
Mini camera lens (Sunex DSL901 12 mm f/3.0 M12 lens)	Sunex, Inc., Carlsbad, CA	http://www.optics-online.com/OOL/DSL/DSL901.PDF
Micro camera lens (Sunex DSL944 7.5 mm f/2.8 M8 lens)	Sunex, Inc., Carlsbad, CA	http://www.optics-online.com/OOL/dsl/dsl944.pdf
Red LEDs (OSRAM LS M67F-S2U2-1-Z 633 nm, 2 mm × 1.4 mm surface mount LED)	Osram Licht AG, Munich, Germany	https://www.digikey.com/en/products/detail/osram-opto-semiconductors-inc/LS-M67F-S2U2-1-Z/2205626
Green LEDs (OSRAM LT M673-P2R1-25-1-10-R18-Z 532 nm, 2 mm × 1.4 mm surface mount LED)	Osram Licht AG, Munich, Germany	https://www.digikey.com/en/products/detail/osram-opto-semiconductors-inc/LT-M673-P2R1-25-1-10-R18-Z/1938806
LED driver (Adafruit 12-Channel 16-bit PWM LED Driver – SPI Interface – TLC59711)	Adafruit, NY, NY	https://www.adafruit.com/product/1455

RESOURCE AVAILABILITY

Lead contact
Further information and requests for resources should be directed to and will be fulfilled by the lead contact, Robert Friedman (friedmro@ohsu.edu).

Materials availability
This study did not generate new unique reagents.

Data and code availability
- All data reported in this paper will be shared by the lead contact upon request.
- All original code has been deposited at DOIs listed in the key resources table and is publicly available.
- Information required to analyze or reanalyze the data reported in this paper is available from the lead contact upon request.

EXPERIMENTAL MODEL AND SUBJECT DETAILS

Animals
All procedures were carried out with the prior approval of the Oregon National Primate Research Center and Oregon Health Sciences University Institutional Animal Care and Use Committee and in accordance with NIH animal welfare guidelines (approval number: IP00111). Two adult female rhesus macaques (*Macaca mulatta*) were used in these studies.

METHOD DETAILS

Animal procedures
For visual cortical areas, our surgical procedures used for implantation of chronic optical chambers, viral vector injections and intrinsic signal optical imaging have been described elsewhere.[17,18,67] These chambers have been described previously,[28] are constructed of plastic, and have been successfully used to image the same cortical location for years.[23,28] In these two animals 5 anesthetized optical intrinsic signal imaging sessions were conducted on three cerebral hemispheres. In brief, during an OISI experiment lasting up to 12 h under anesthesia, an animal was induced with ketamine, positioned in a stereotaxic fame, mechanically respired and anesthetized for OISI with propofol (5–15 mg/kg/h, CRI) and ketamine (10–25 μg/kg/min, CRI). Vital signs such as heart rate, blood oxygen saturation, expired carbon dioxide concentration, electrocardiogram, blood pressure and temperature were monitored. Speculums were placed in the eyes and contact lenses were used to focus vision on a computer monitor 57 cm away. In one of these animals, we conducted awake OISI on two cerebral hemispheres and combined optogenetic stimulation with OISI on one cerebral hemisphere with chronic optical windows implanted over V1, V2 and V4. During ~3-h sessions of awake OISI, the animal was placed in a primate chair and presented with visual and optogenetic stimuli without requiring eye fixation or performance on a behavioral task.

Chamber maintenance
After a durotomy a thermoplastic polyurethane (Tecoflex®) artificial dura (AD) is placed such that the brim of the AD ''hat'' is tucked under the dura as described previously.[28] This material is biologically inert and seems to minimize any reactive tissue response. After

1 week with the Tecoflex AD the cortical surface is less susceptible to a reactive response and we replace the Tecoflex AD with a silicon AD as described previously.[67] The silicone AD is less rigid and can form a more airtight seal with the chamber walls, which results in slower regrowth of the dura. Chamber cleaning is performed biweekly when no recordings were underway or following every recording session. Between cleanings, since the AD maintains a barrier between the brain and chamber, we place in the chamber a small piece of gauze with a drop of antibiotic (ophthalmic gentamycin or ceftriaxone) to soak up any fluid collection in the chamber and prevent infection. The outside of the chamber is cleaned with alternating disinfectant solutions (betadine, chlorhexidine, and 70% ethanol) prior to removing the chamber cap. Using sterile technique, the gauze is removed with forceps, the inside of the chamber is rinsed multiple times with sterile saline, and a new piece of gauze infused with a few drops of antibiotic is placed on top of the AD. The chamber is sealed closed with a sterile chamber cap. The outside of the chamber is once again cleaned with a disinfectant solution (betadine, chlorhexidine, or 70% ethanol).

Viral vector injection

A 200 μm Hamilton syringe was used to inject an adenoviral vector AAV9-CaMkII-hChR2(H134R)-EYFP[66] into one color and one orientation domain in V2 and one orientation domain in V4 as well as AAV5-CaMkII-hChR2(H134R)-EYFP[66] into one color and one orientation domain in V4 (Figure S6). Once the target domains were chosen, we overlaid their locations onto a vessel map of the brain (Figure S6D), which we used to target the viral injections. At each site, 0.5 μL injections were made at three cortical depths (1.2, 0.8, and 0.4 mm). Injections were performed at individual depths over 5 min after which there was an additional 10 min pause before repositioning the syringe. Fluorescence of enhanced yellow fluorescent protein (EYFP), first monitored at 6 weeks, was used to indicate successful transfection at injection sites. After a six-week incubation time, robust expression was seen around all five of our injection sites (Figure S6F). We observed that expression of the AAV9 virus appeared visually stronger than the expression of the AAV5 virus.

Wireless μLED configuration

A commercially available wireless μLED system was used for these studies (Neurolux, Inc, Northfield, IL; see Shin et al.[29] for details). The wireless μLED implant contained a 10 or 16 mm in diameter inductively coupled receiver coil, etched on a thin flexible polyimide substrate, which powered via a low dropout voltage regulator a 270 by 220 by 50 μm μLED chip (470 nm center wavelength). The implant was laid flat facing cortex on top of the silicon artificial dura hat (which is optically clear) and held in place by the pressure of the cover glass (which creates a flattened imaging FOV and minimizes cortical pulsation). The μLED implant and its corresponding ring obscures cortex in the FOV and can produce a very small shadow on cortex and a fair amount of reflection of the light from the LEDs used to illuminate cortex (see Figure 5B). Strategic positioning of the μLED ring and utilization of a larger 16 mm diameter receiver coil were approaches used to reduce the amount of obscured cortex in areas of interest. Stabilizing cortex with a cover glass reduced the impact of reflection and shadows in the OISI subtraction maps.

The power was provided by an antenna positioned above and around the head of the animal. The transmitting antenna consisted of two circular loops of 22 gauge wire supported by a 3D printed plastic cage. It was tuned to 13.56 MHz using a jumper-based resistor capacitor box provided by NeuroLux. The 13.56 MHz frequency was used because it is the base frequency of the near field communication or NFC protocol, which is a fairly mature technology used in cell phones as well as credit cards for both remote power and communication. The resonance was tested using an antenna analyzer (RigExpert AA-170, Rig Expert Ukraine Ltd., Kyiv, Ukraine) to make sure that the standing wave ratio was less than 1.3. Power produced by the μLED was measured using an optical power and energy meter (PM100D, Thorlabs Inc., Newton, NJ) with a standard photodiode power sensor (S120C, Thorlabs Inc). Several antenna designs were evaluated each aimed at minimizing obstruction to the visual field of the animal while maintaining power delivery to the implant (3D designs available, see and key resource table). The software and hardware provided by the NeuroLux system included programmable pulse rate and duty cycle, as well as pulse train duration of the μLED. The estimated temperature rise in tissue by μLED stimulation at the irradiances ($\sim$1–10 mW/mm^2) and μLED thermal efficiency of 33% used in these studies would, based on modeling, be less than 0.1°.[68]

To evaluate whether potential animal movement would affect the output of the μLED, we attached it to a single-chip triple-axis accelerometer (MPU-6050, InvenSense Inc., Sunnyvale, CA) running at 20 Hz while measuring the optical output of the μLED via a flexible 1 mm diameter fiberoptic cable coupled to an amplified photodiode (PDA100A, Thorlabs Inc). Optical measurements and acceleration forces on the implant were collected via a serial interface at 16-bit resolution. The implant was then manually shaken while being powered by the antenna. Acceleration forces produced by natural head movements were collected by mounting the accelerometer to the head implant while the animal was seated in a primate chair.

Optogenetic stimulation

Within the optical chamber the implant was affixed in place with a small amount of clear agar and a clear polycarbonate disc, which also served to flatten the cortical surface, minimize brain movement during imaging, and provide an imaging window. Pulse trains with a frequency of 24 Hz were delivered to the 470 nm blue μLED with an optical power of 2 mW. Pulse width was 20 ms and stimulus length varied between 300, 600, and 900 ms. With the red LEDs used for illumination of cortex (625 nm, bw +/− 10 nm; https://cree-led.com/media/documents/XLampXPE-25A.pdf) intrinsic imaging would not interfere with optogenetic stimulation given the minimal overlap with the action spectrum of channelrhodopsin.[69] The green LED (520–530 nm) used to collect a cortical blood vessel

image for image registration falls within the activation spectrum for channelrhodopsin; however, green LED illumination was performed either before or after intrinsic imaging data collection. During OISI of µLED stimulation, stimulation conditions and blank trials were pseudorandomly interleaved with an 8 s interstimulus interval, while the monkey looked at a neutral gray computer monitor.

Visual stimuli

For anesthetized OISI, visual stimuli consisted of square wave and sine wave full screen gratings with spatial frequencies of 2° per cycle that moved at a rate of 2 cycles per second, presented to one eye through a pair of electromechanical shutters. Visual stimuli with presentation durations of 4 s were generated using a ViSaGe MKII Stimulus Generator (Cambridge Research Ltd, UK). In the imaging runs designed to reveal ocular dominance columns in V1 and functional orientation domains, and borders of visual areas, four different orientations (0°, 45°, 90°, and 135°) of high contrast square wave achromatic gratings were presented separately to each eye. To reveal color domains, two different orientations (45 and 135°) of isoluminant red/green and achromatic luminance sine wave gratings were presented to the eye contralateral to the cortex being imaged. To reveal ocular dominance columns with OISI in the awake animal, a 10-min video of conspecific grooming was shown to each eye. During imaging of optogenetic stimulation the animal was presented with a neutral gray screen.

QUANTIFICATION AND STATISTICAL ANALYSIS

SNR_{MAX} measurement

To obtain empirical measurements of the signal to noise near pixel saturation levels of illumination (measured SNR_{MAX} in Table 1), we measured RMS signal variance of superpixels (after frame binning and pixel binning) for each camera. Identical illumination was provided by a 630 nm (red) LED. The object imaged was an artificial cortex (Optical Imaging, Rehovot 76701, Israel) consisting of red LEDs behind an opaque filter (to diffuse hot spots) that was provided to test the sensitivity of the benchtop system. We acquired 1000 imaging frames (after frame binning to 5 fps) from each camera. The length of each exposure varied from camera to camera so that each camera sensor was near saturation under identical lighting conditions. SNR tests of the camera under ring illumination lighting were similar to those conducted with the single LED illumination of cortex used in our benchtop studies.

Optical intrinsic signal imaging

For a detailed description of the OISI approach see.[23,24,67] In brief, to create an optical window during anesthetized OISI prior to chamber implant, exposed cortex was covered with a 4% agar saline solution and stabilized with a glass coverslip. For chamber imaging, a threaded ring secured a Plexiglas disk to reduce cortical pulsations and create an optical window. Blood vessel maps were taken under green light (532 nm) illumination and OISI was done under red light (630 nm) illumination. Images of tissue reflectance, the change in which constitutes the intrinsic hemodynamic signal and correlated with local cortical activity,[27] were collected with three different cameras (Table 1). Imaging obtained with the Dalsa CCD camera (1M60P, Teledyne DALSA, Canada) was collected with a benchtop Imager 3001 system (Optical Imaging Ltd., Rehovot 76701, Israel). Imaging from two XIMEA cameras (MC023MG-SY and MU9PM-MH, XIMEA GmbH, Münster, Germany) was collected using custom software written in the Python scripting language using the xiAPI Python interface (https://www.ximea.com/support/wiki/apis/Python). For the XIMEA cameras, proper focus and exposure were determined using the XIMEA CamTool software. Frames were collected at the maximal frame rate for each camera (Table 1) that allowed summation to create binned 5 frames-per-second image sequences. In tests comparing camera performance no changes to lighting were made between imaging runs with the different camera and lens combinations. Instead, camera exposure time was varied to bring illumination to near saturation levels as generally performed during OISI.

For episodic OISI visual stimulation or optogenetic experiments, changes in cortical reflectance were calculated by subtracting from each imaging frame the average of 1 or 2 imaging frames acquired just prior to stimulus onset. To increase signal to noise, stimuli were repeated 20 times for ocular dominance (OD) imaging and 40 times for monocular color domain imaging runs (this means that the same number of trials was used to generate color maps and OD maps). Trials were repeated 20 times during the optogenetic stimulation OISI runs. During awake ocular dominance runs a 10-min video (3000 imaging frames) was shown to each eye once with a 15 s interstimulus interval. All 3000 imaging frames were summed together and the sum from left eye viewing was subtracted from the sum from right eye viewing to create the ocular dominance map. For image display, images were spatially filtered using a mean filter approach with low pass filters set from 2 to 6 pixels and high pass filters set 90 to 200 pixels, and the range of pixel values clipped with a SD of 1.5–2.5 (depending on the strength of the signal). T-maps, generated by pixel-by-pixel Student's t-tests, were used to statistically identify locations of stimulus-related response. T-maps were generated with MATLAB (The Mathworks, Inc, Natick, MA) and were visualized by creating maps thresholded for a specific p value (i.e., $p < 0.01$).